Eur. Phys. J. D **39**, 359–371 (2006)
DOI: 10.1140/epjd/e2006-00120-5

THE EUROPEAN PHYSICAL JOURNAL D

A comparative nearside-farside analysis of the He–N_2^+ and He–N_2 inelastic collisions

G. Guillon and T. Stoecklin[a]

Université de Bordeaux 1, UMR5803-CNRS, 351 cours de la Libération, 33405 Talence Cedex, France

Received 3 November 2005 / Received in final form 20 January 2006
Published online 7 June 2006 –

Abstract. A comparative study of the inelastic scattering of $^{14}N_2^+$ and $^{14}N_2$ in collision with ^{3}He atoms is presented. The unrestricted nearside-farside (NF) method proposed by Connor [J. Chem. Phys. **104**, 2297 (1995)] is applied to analyse the Close Coupling rotationally state selected angular distributions for four kinetic energies. These four energies illustrate different regimes of the dynamics. The relationships between the structures of the calculated differential cross-sections (DCS) and the different regions of the potential energy surfaces involved which can be extracted from semi classical models are here easily obtained from a simple reading of the (NF) figures. At the higher energy far-off the wells (1000 cm^{-1}) the shape of the DCS are quite similar for the two systems and their nearside-farside components also, showing that the inelastic process is controlled by the short range repulsive part of the potential which is essentially the same for these two collisions. When the energy is decreased the differences between the two wells associated with the He–N_2^+ and He–N_2 complexes are responsible for the differences between the DCS for the two systems. The farside component associated with the well become more and more prominent for the elastic scattering while inelastic scattering remains controlled by the repulsive core in a large angular interval. The nearside farside analysis gives also a new picture of a resonance which is regarded as an equilibrium between the repulsive and the attractive parts of the potential.

PACS. 34.50.-s Scattering of atoms and molecules – 34.50.Ez Rotational and vibrational energy transfer – 34.50.Pi State-to-state scattering analyses – 03.65.Sq Semiclassical theories and applications

1 Introduction

The determination of precise inelastic scattering cross-sections and rate coefficients is very important in astrochemistry [2] where they are used to estimate the molecular abundances of the detected species. They are also needed in order to optimise the cooling and trapping of molecules which is a very active new field [3] where the tuning of the interaction potential using external fields is hoped to allow controlling chemical reactions [4]. Since the accuracy of these calculations relies on the quality of the potential energy surfaces, both the comparison with the experimental data available and the design of new tools allowing analysing the influence of the different parts of the PES are necessary. A good example illustrating this last point can be found in rotationally state selected differential cross-sections (DCS) which give some of the most detailed information about the role played by each part of the PES. Experimental observation of rainbow effect for the rotationally elastic DCS provided for example early evidence for the existence of Van der Waals potential well for non reactive systems. Very often, however the angular scattering of elastic and inelastic collisions is highly structured and difficult to analyse. In a series of recent papers, Connor [1,5–7] adapted the nearside farside (NF) method to atom diatom inelastic scattering and showed that it is an efficient way to extract physical insight from a close coupling computation of the DCS. This technique was originally introduced into nuclear heavy-ion scattering for Legendre partial wave series (PWS) by Fuller [8] and later by Hatchell [9]. The NF analysis is based on the decomposition of the scattering amplitude into two subamplitudes. The nearside amplitude which should include all the scattering from the nearside of the target and the farside amplitude which should include all the farside scattering. Structure in the angular distribution can arise from each of the two subamplitudes or from their interferences and can then be analysed in terms of their links with the different parts of the potential energy surface involved.

In two recent studies we calculated the integral rovibrationally inelastic scattering cross-sections for the He–N_2 [10] and He–N_2^+ [11] collisions. We found some striking differences between the dynamical behaviours for these two systems as a result of the differences between the PES associated with these two collisions. As a matter of

[a] e-mail: t.stoecklin@lpcm.u-bordeaux1.fr

fact, the well associated with the He–N_2^+ complex is four time deeper than its neutral counterpart and the long rage part of the two potential energy surfaces are also quite different (charge induced dipole for He–N_2^+ and dispersion for He–N_2). In the present study we will extend this analysis to rotationally state selected differential cross-sections. In the next section the main steps of the NF analysis will be reminded and the main features of the potential energy surfaces used will be briefly described. The parameters of the close coupling calculations will be given for both systems. The results of the calculations will then be discussed in Section 3.

2 Computation methodology

In this study we use the most detailed version of the NF analysis which utilizes the helicity representation of the scattering amplitude and is valid for general state to state inelastic scattering of the type:

$$A + BC(j_i, m_i) \Rightarrow A + BC(j_f, m_f)$$

where j_i, j_f are the rotational angular momenta of the diatomic molecule before and after the collision and m_i, m_f are respectively their projections along the intermolecular axis. Since we will present only rotational transitions inside the fundamental vibrational level of the diatomic molecules ($\nu_i = \nu_f = 0$), these labels will be omitted from now on, to keep the notation as simple as possible. This method was first introduced and detailed very clearly by Connor in reference [7], and therefore the main steps of the method will only be reminded.

We start from the usual expression of the helicity scattering amplitude [12] as a function of the body fixed scattering matrix $S^J_{j_i,m_i\to j_f,m_f}$:

$$f_{j_i,m_i\to j_f,m_f}(\theta) = \frac{1}{2ik_{j_i}} \sum_{J=\max(|m_i|,|m_f|)}^{\infty} (2J+1) \times \left[S^J_{j_i,m_i\to j_f,m_f} - \delta_{j_i,j_f}\delta_{m_i,m_f}\right] d^J_{m_i,m_f}(\theta) \quad (1)$$

where θ is the scattering angle, J the total angular momentum $d^J_{m_i,m_f}(\theta)$ is a reduced rotation matrix and k_{j_i} the translational wave number for the relative motion in the initial channel. In this expression a constant phase factor has been ignored.

The differential cross-section is then

$$I_{j_i,m_i\to j_f,m_f}(\theta) = \left|f_{j_i,m_i\to j_f,m_f}(\theta)\right|^2 \quad (2)$$

and this expression is summed in order to obtain the degeneracy averaged differential cross-section:

$$I_{j_i\to j_f}(\theta) = \frac{1}{(2j_i+1)} \sum_{m_i=-j_i}^{j_i} \sum_{m_f=-j_f}^{j_f} I_{j_i,m_i\to j_f,m_f}(\theta). \quad (3)$$

The NF decomposition [7] is obtained from the expansion of the Wigner matrices into travelling wave components:

$$d^J_{m_i,m_f}(\theta) = d^{J(+)}_{m_i,m_f}(\theta) + d^{J(-)}_{m_i,m_f}(\theta) \quad (4)$$

where

$$d^{J(\pm)}_{m_i,m_f}(\theta) = \frac{1}{2}\left[d^J_{m_i,m_f}(\theta) \mp \frac{2i}{\pi} e^J_{m_i,m_f}(\theta)\right] \quad (5)$$

and the $e^J_{m_i,m_f}(\theta)$ functions were defined and named by Connor [7] reduced rotation matrices of the second kind. These functions were designed in order to make the $d^{J(\pm)}_{m_i,m_f}(\theta)$ behave asymptotically (for big values of J) like angular waves moving in the clockwise and anticlockwise directions. A semi classical analysis [13] of the (+) and (–) components shows that these waves respectively can be interpreted as originating from the farside (F) and the nearside (N) of the target. The nearside farside decomposition of the scattering amplitude is obtained by substituting expression (4) in equation (1),

$$f_{j_i,m_i\to j_f,m_f}(\theta) = f^{(+)}_{j_i,m_i\to j_f,m_f}(\theta) + f^{(-)}_{j_i,m_i\to j_f,m_f}(\theta) \quad (6)$$

where

$$f^{(\pm)}_{j_i,m_i\to j_f,m_f}(\theta) = \frac{1}{2ik_{j_i}} \sum_{J=\max(|m_i|,|m_f|)}^{\infty} (2J+1) \times \left[S^J_{j_i,m_i\to j_f,m_f} - \delta_{j_i,j_f}\delta_{m_i,m_f}\right] d^{J(\pm)}_{m_i,m_f}(\theta). \quad (7)$$

If the expression (6) is substituted in the expression (2) of the differential cross-section an interference term between the two sub amplitudes is obtained which is important in angular intervals where the two subamplitudes are of the same order of magnitude and the structure in the angular distribution can then arise from each of the two sub amplitudes or from their interferences. One has also to keep in mind that the semi classical interpretation in terms of clockwise and anticlockwise waves is obtained from the asymptotic behaviour of the $d^{J(\pm)}_{m_i,m_f}(\theta)$. The low J terms in the expansion of the differential cross-section do not follow this asymptotic behaviour and can when they are numerically significant alter the semi classical interpretation of the structures of the angular distribution. Furthermore, the NF decomposition is meaningless when the NF angular distributions are more structured than the DCS.

3 Calculations

3.1 The He–N_2 and He–N_2^+ potential energy surfaces

Both systems have been the subject of numerous studies [14–18]. However none of them were dedicated to angular distributions. We calculated for both systems new surfaces in recent works [10,11] dedicated to the study of the vibrational quenching of the $\nu = 1$ state of these two diatomic molecule. Both surfaces are based on large grids of ab initio points calculated respectively at the

coupled cluster BCCD(T) and the MRCI level using an aug-cc-pVQZ basis set [19]. The analytical models of the potential energy surfaces were constructed using the reproducing kernel Hilbert space method [20] which has proved to be very effective for the description of several van der Waals systems including He–HF [21], He–F_2 [22] and H–F_2 [23] which we also studied. One important aspect of this method is that the asymptotic behaviours of the reproducing kernel functions are known analytically and allow to describe exactly the long range part of the potential which differ strongly for these two systems: (dispersion for He–N_2 and charge induced dipole for He–N_2^+).

We found that the T-shaped structure is the most stable for both Van der Waals complexes. The well depth value and the geometry in Jacobi coordinates associated with these intermediates are respectively: $D_e = -21.651$ cm^{-1} and ($R = 6.4775a_0$, $r = 2.0743a_0$, $\theta = 90°$) for He–N_2 and $D_e = -84.4590$ cm^{-1} and ($R = 6.08a_0$, $r = 2.11a_0$, $\theta = 90°$) for He–N_2^+. The geometries of the two intermediates are then quite similar, while the well associated with the ionic complex is four time deeper than its neutral equivalent. These strong differences in both the intermediate energy and the long range parts of the PES are expected to be revealed by the nearside farside analysis.

3.2 Dynamics

We performed close coupling calculations using our code. This program is based on the Magnus propagator introduced by Light and coworkers [24]. The scattering equations are propagated in the spaced fixed coordinates and the asymptotic matching to diagonal spherical Bessel functions of the first and second kind follows the lines described by Launay [25].

We included 15 ortho rotational states in the basis set for the vibrational level $\nu = 0$ considered in the calculations. This means that at the highest collision energy considered (1000 cm^{-1}) we included four closed channels. The maximum propagation distance was 300 Bohr and convergence was checked as a function of the propagator step size. The convergence of the cross-section was also checked as a function of the total angular momentum for each value of the kinetic energy. The maximum value of total angular momentum J used in the calculations was $J = 50$. At each point of the propagation grid the matrix elements of the potential were evaluated using the ground state vibrational wave function considered in the calculation and expanding the potential in Legendre polynomials retaining terms respectively up to $l = 8$ for He–N_2 and $l = 12$ for He–N_2^+ on a grid of 8 points used to calculate the Gauss Hermite quadrature of the vibrational part of the integral. A discrete variable representation (DVR) along the Gauss Hermite grid of the diatomic rovibrational wave functions was calculated by solving the exact diatomic equations using the diatomic potential described in our previous work [10,11] and a finite basis representation (FBR) of 150 imaginary exponential wave functions as described for example by Colbert and Miller [26].

The body fixed S matrix elements necessary to calculate the helicity scattering amplitude are then obtained from the Space Fixed ones by [25]:

$$S^J_{j_i,m_i;j_f,m_f} = \sum_{l_i=|J-j_i|}^{J+j_i} \sum_{l_f=|J-j_f|}^{J+j_f} i^{[l_i-l_f]} \times \langle j_i m_i, J-m_i | l_i 0\rangle \langle j_f m_f, J-m_f | l_f 0\rangle S^J_{j_i,l_i;j_f,l_f}. \quad (8)$$

We then generated the reduced rotation matrices $e^J_{m_i,m_f}(\theta)$ using the algorithm provided by Connor in reference [7] and checked our code using the numerical checks proposed by him in the same paper. We then obtained straightfully the nearside and farside components of the scattering amplitude.

4 Results and discussion

We selected four collisions energies. The lowest energy 4.98×10^{-3} cm^{-1} is the position of a pure shape resonance for the ^{3}He–N_2^+ collision without equivalent for the ^{4}He–N_2^+ collision [11]. This unusual feature will allow us to discuss the picture of a resonance given by the nearside farside analysis. The second energy 20 cm^{-1} is slightly below the well depth associated with the He–N_2 complex. The third 100 cm^{-1} is moderately above the well depth associated with the He–N_2^+ complex and the last energy 1000 cm^{-1} is large compared to both well depths. In all the figures apart the one dedicated to the resonance, the curves associated with the He–N_2^+ and He–N_2 collisions will be respectively presented on their left and right side. We will also draw both nearside and farside components as well as the usual state selected differential cross-section. We use the unrestricted nearside farside analysis which is known to produce nearside and farside cross-sections which are larger than the real DCS for some transitions and in some angular range around the forward or backward directions. This drawback which has been discussed by Connor can be corrected [7]. It is due to caustics associated with the $d^J_{m_i,m_f}(\theta)$ and $e^J_{m_i,m_f}(\theta)$ at $\theta = 0$ and $\theta = \pi$; and will not affect our discussion outside these very narrow angle intervals. At each energy we will discuss successively the purely elastic transitions, those elastic in j and inelastic in m, those elastic in m and inelastic in j, those inelastic in both j and m and those degeneracy averaged.

4.1 E = 1000 cm^{-1}

If we fist consider in Figure 1 the purely elastic collisions, we see that for the He + N_2^+ collision the angular distributions are forward peaked and that the nearside and farside components are of the same order of magnitude at this energy. They both present fast oscillations which are of great amplitude for the nearside component and small amplitude for the farside component, the constructive and destructive interferences between the two subamplitudes yielding fast oscillations of big amplitude of the

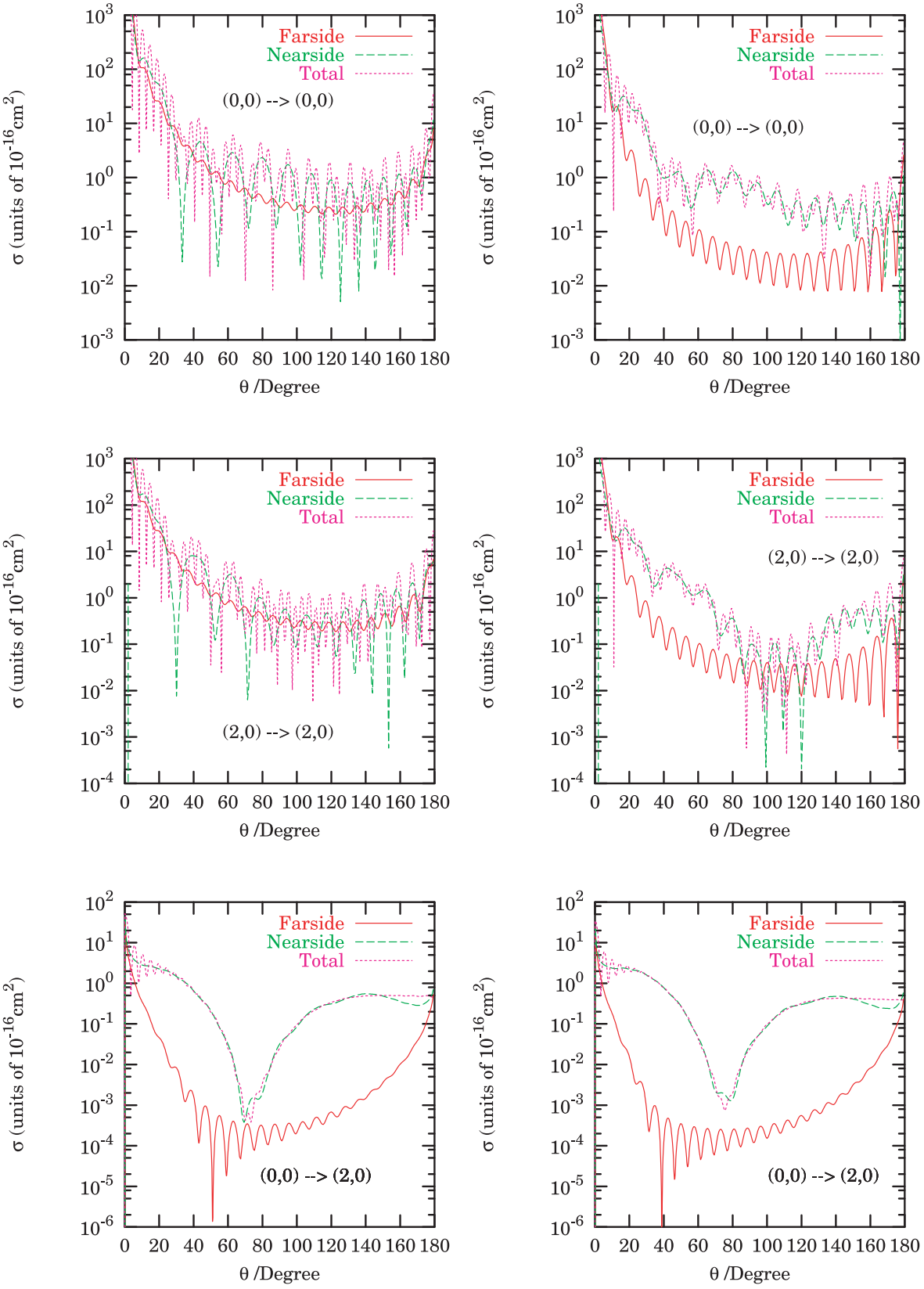

Fig. 1. (Color online) Differential cross-sections at $E = 1000$ cm^{-1}, $\log(I(\theta))$ versus θ for the transitions ($\Delta j = 0$, $\Delta m = 0$) and ($\Delta j \neq 0$, $\Delta m = 0$) as indicated in the figure in the He–N_2^+ and He–N_2 collisions. The collisions involving N_2^+ and N_2 are respectively on the left side and right side of the figure.

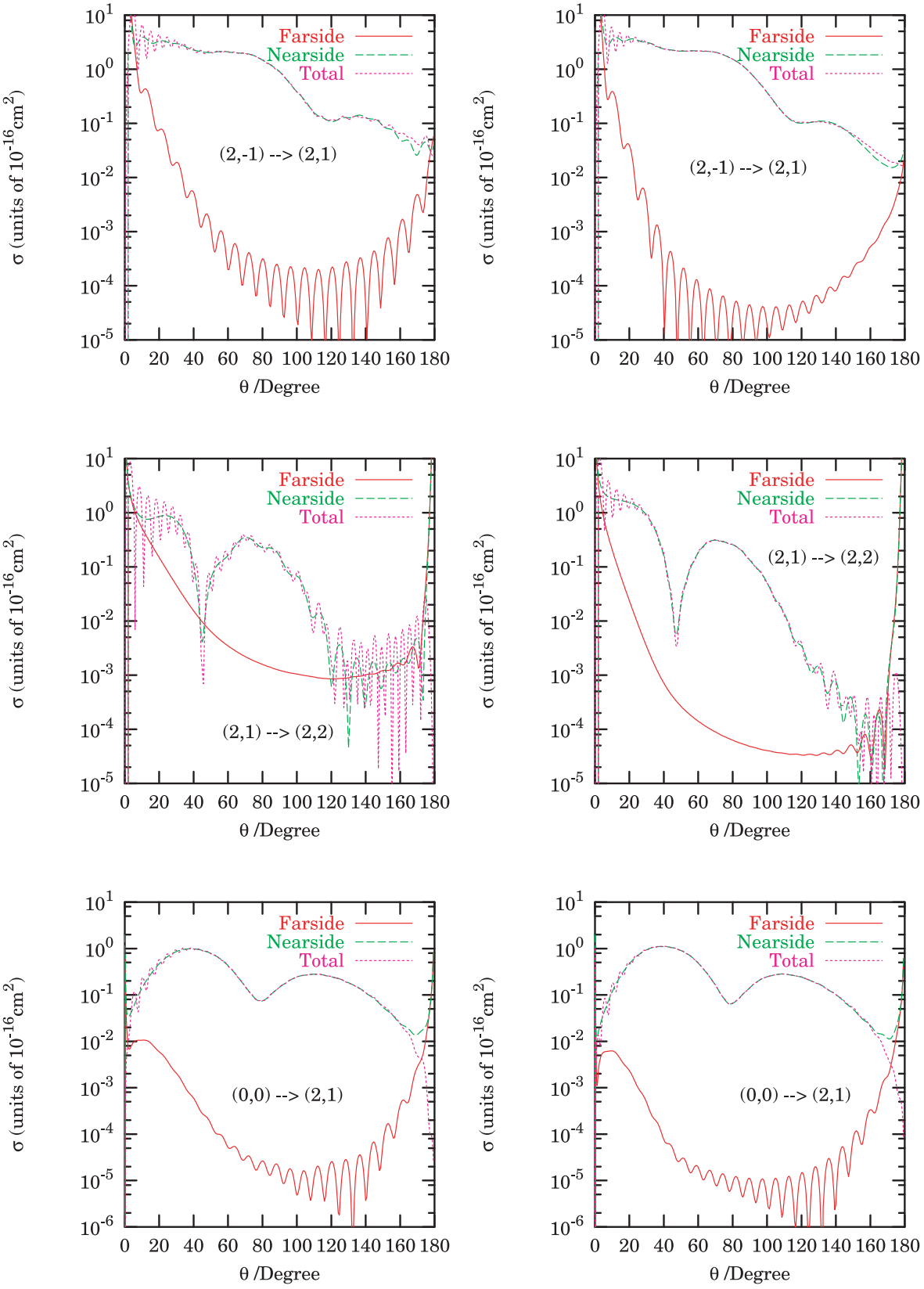

Fig. 2. (Color online) Differential cross-sections at $E = 1000$ cm^{-1}, $\log(I(\theta))$ versus θ for purely inelastic transitions (as indicated in the figure) in the He–N_2^+ and He–N_2 collisions. The collisions involving N_2^+ and N_2 are respectively on the left side and right side of the figure.

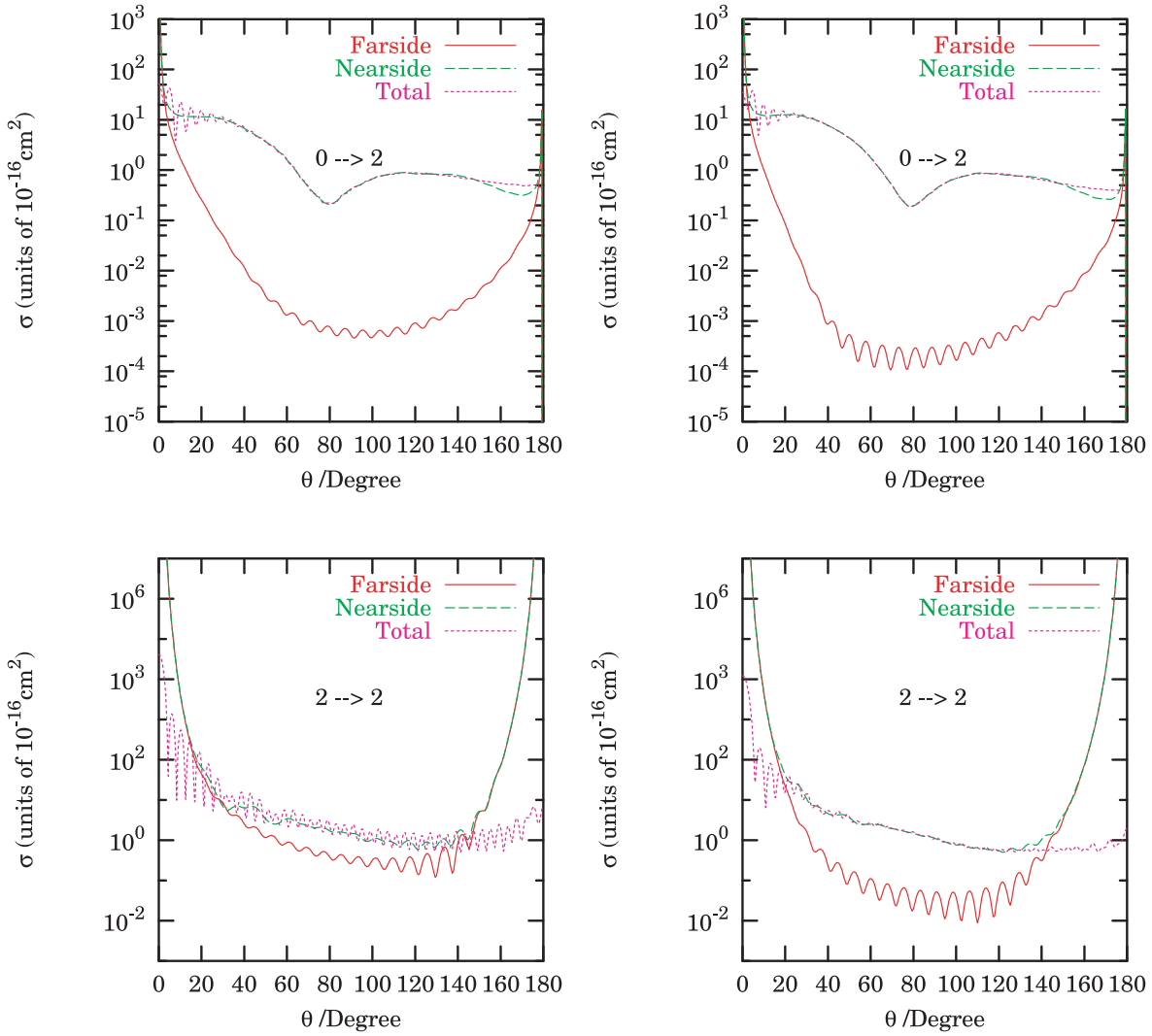

Fig. 3. (Color online) Degeneracy averaged differential cross-sections at 1000 cm^{-1}, $\log(I(\theta))$ versus θ for the transitions indicated in the figure in the He–N_2^+ and He–N_2 collusions. The collisions involving N_2^+ and N_2 are respectively on the left side and right side of the figure.

differential cross-section. If we compare on the same figure these features with those associated with the He–N_2 collision, we already see a difference between the two systems. As a matter of fact, if the general profiles of the DCS are similar, the nearside component is slightly larger than the farside component, showing that the collision involving neutral N_2 is controlled by the repulsive part of the potential at this energy.

If we now consider inelastic transitions, the nearside component is always larger than its farside counterpart now for both the neutral and the ionic systems as can be seen in Figures 1 and 2 where the DCS associated with transitions elastic in m and inelastic in j, elastic in j and inelastic in m and purely inelastic are reported. The similarities between the curves associated with the neutral and the ionic collisions are really striking for the $\Delta m = 0$ inelastic transitions represented in Figure 1. The familiar profile of the Rainbow [27] scattering is now apparent on both nearside and farside components. The oscillations of the farside subamplitude are faster and the position of the main rainbow shifts to bigger angle as the rotational inelasticity Δj increases. This is usual for Rainbow scattering and is exemplified in Figure 2. One clearly sees also in Figure 2 that the number of oscillations of the nearside component decreases as Δm increases and $\Delta j = 0$ while the number of oscillations of the farside component increases.

The degeneracy averaged angular distributions which are independent of the direction chosen for the quantization axis are reported in Figure 3. They produce a simpler scattering pattern. The diffraction oscillations [28] are easier to identify in a narrow angular interval close to $\theta = 0$ limited to the region where the two subamplitudes have comparable magnitudes for the transition $j = 0 \rightarrow j' = 2$. The strong divergence in the forward and backward directions of the nearside and farside components of the DCS associated with the $j = 2 \rightarrow j' = 2$ transition which can be seen in the same figure are meaningless. As mentioned

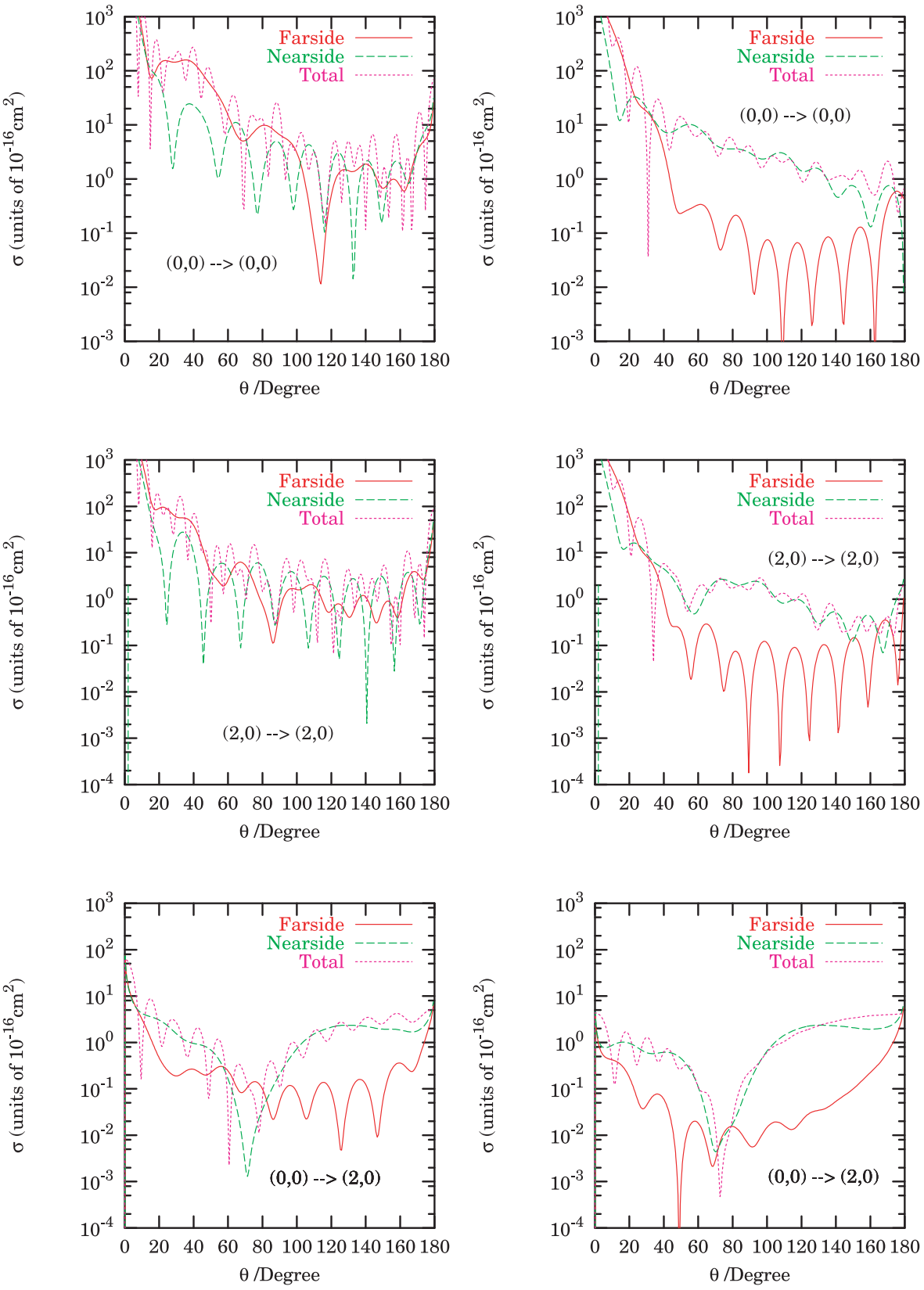

Fig. 4. (Color online) Differential cross-sections at 100 cm^{-1}, $\log(I(\theta))$ versus θ for the transitions ($\Delta j = 0$, $\Delta m = 0$) and ($\Delta j \neq 0$, $\Delta m = 0$) as indicated in the figure in the He–N_2^+ and He–N_2 collusions. The collisions involving N_2^+ and N_2 are respectively on the left side and right side of the figure.

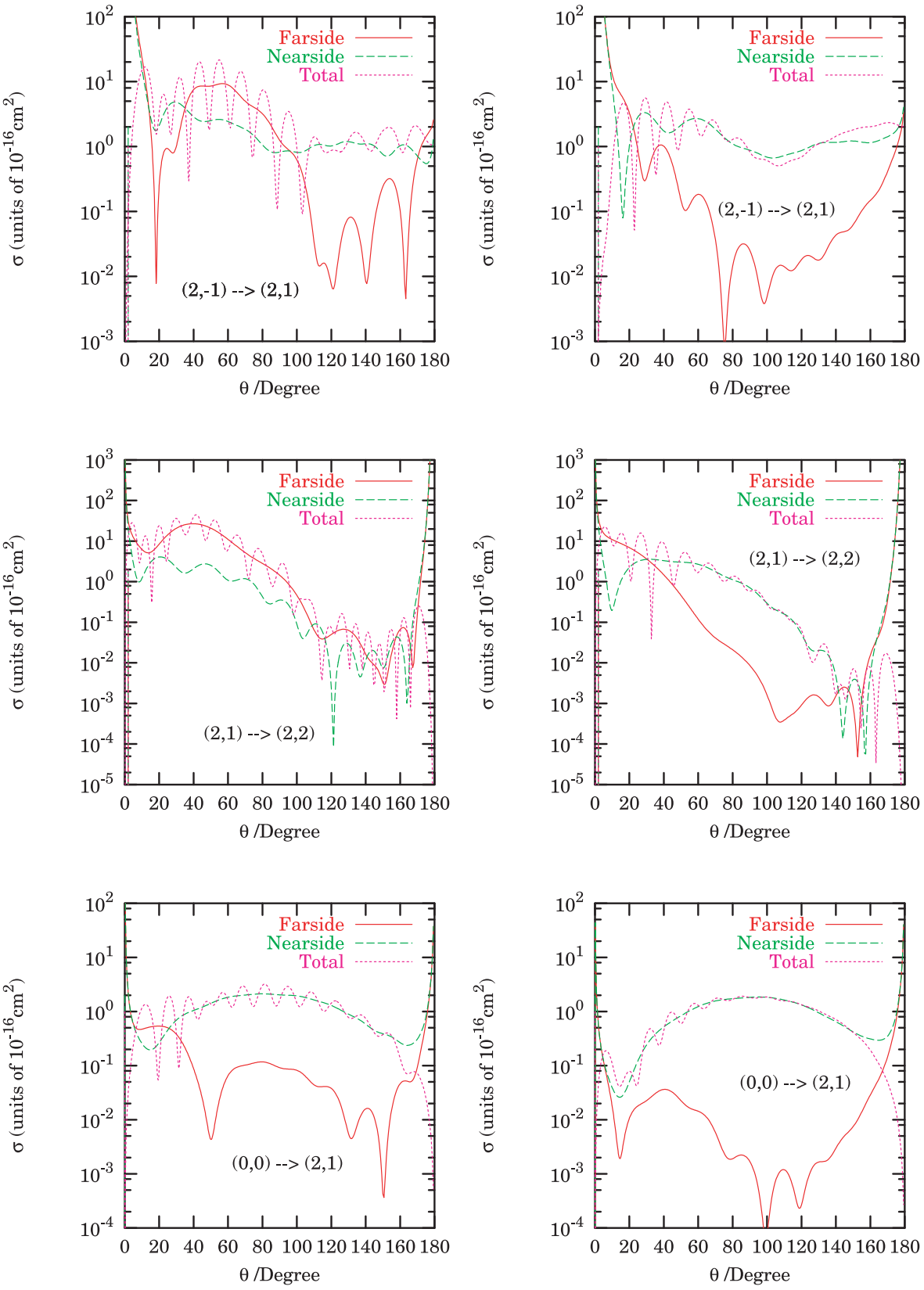

Fig. 5. (Color online) Differential cross-sections at $E = 100\ \mathrm{cm}^{-1}$, $\log(I(\theta))$ versus θ for purely inelastic transitions (as indicated in the figure) in the He–N_2^+ and He–N_2 collisions. The collisions involving N_2^+ and N_2 are respectively on the left side and right side of the figure.

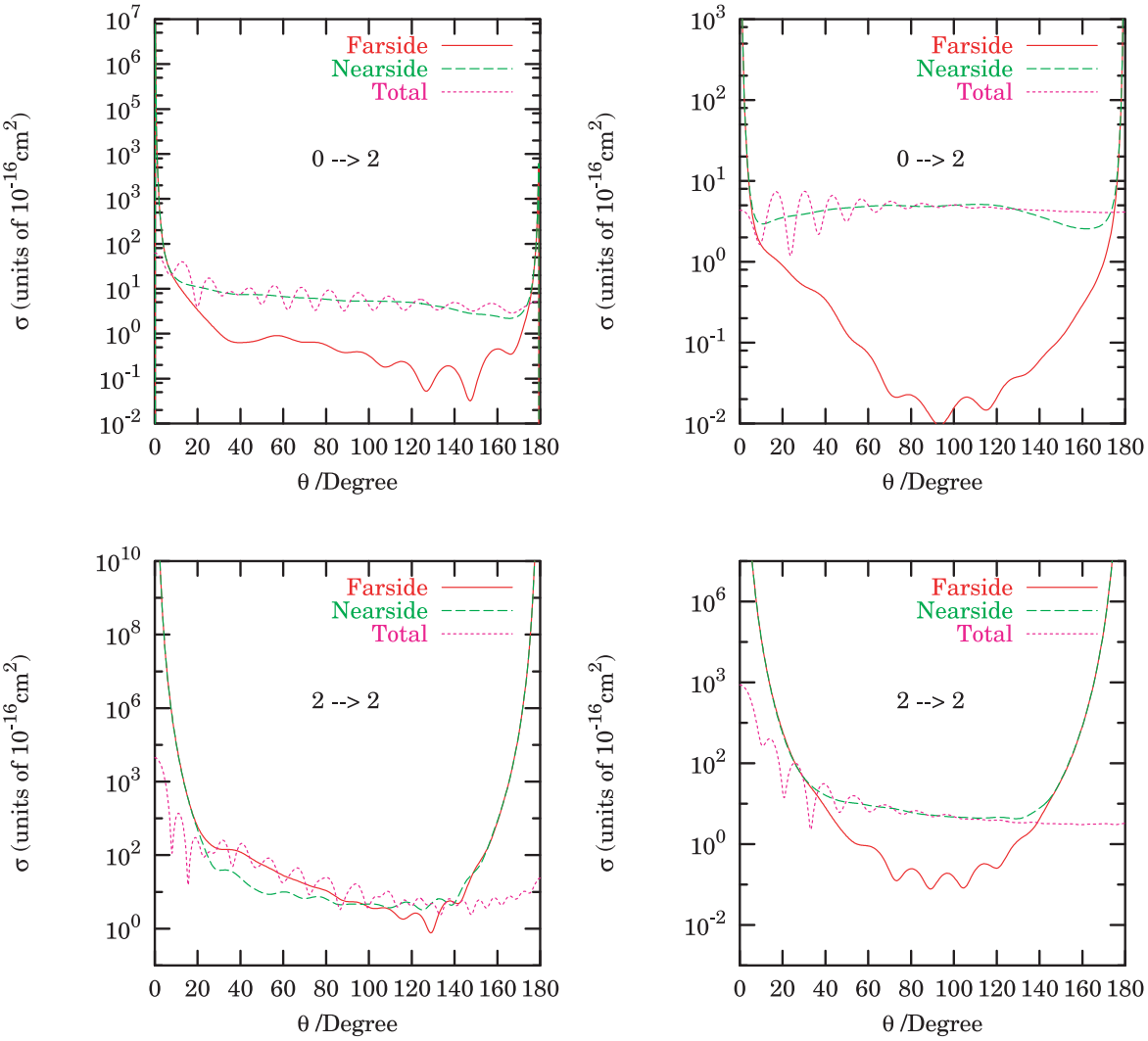

Fig. 6. (Color online) Degeneracy averaged differential cross-sections at 100 cm^{-1}, $\log(I(\theta))$ versus θ for the transitions indicated in the figure in the He–N_2^+ and He–N_2 collisions. The collisions involving N_2^+ and N_2 are respectively on the left side and right side of the figure.

previously, they are due to the caustics of the $d^J_{m_i,m_f}(\theta)$ and $e^J_{m_i,m_f}(\theta)$ at $\theta = 0$ and $\theta = \pi$ and the travelling wave interpretation is no longer valid in these intervals.

4.2 E = 100 cm^{-1}

If we consider again first the elastic transitions for the He + N_2^+ system we see in Figure 4 that both nearside and farside components are equally important as in the case of the previous energy. However the amplitudes of the oscillations of the two components which were very different at 1000 cm^{-1} are now comparable. Furthermore, the farside subamplitude at this energy exhibits clearly a slowly oscillating rainbow profile. As we know from a semi classical approach the rainbow in elastic scattering differential cross-sections reflects the presence of a minimum in the potential [29] and this structure is then a result of the presence of the well associated with the He–N_2^+ complex. If we now consider on the same figure the elastic transitions curves for the neutral system we see that at this energy the nearside component associated with the repulsive part of the potential still controls the collision for a large domain of angle. This is not surprising since the depth of the well associated with the He–N_2 complex is still small compared to the collision energy. There are however now two distinct regimes. In the forward direction the collision is now controlled by the farside component up to 30°.

When one considers the inelastic transitions in Figures 4 and 5 for both the neutral and the ionic collision, one clearly sees the farside component getting closer in amplitude to its nearside counterpart and exhibiting a Rainbow profile which was not as obvious at 1000 cm^{-1}. While the nearside component almost did not change, the oscillations of the farside component become slower and have grown in amplitude. This shows the increase effect of the well and even in some cases (compare Figs. 5 and 2) the farside component now controls the collision involving N_2^+ at 100 cm^{-1} when it was negligible compared to the nearside component at 1000 cm^{-1}.

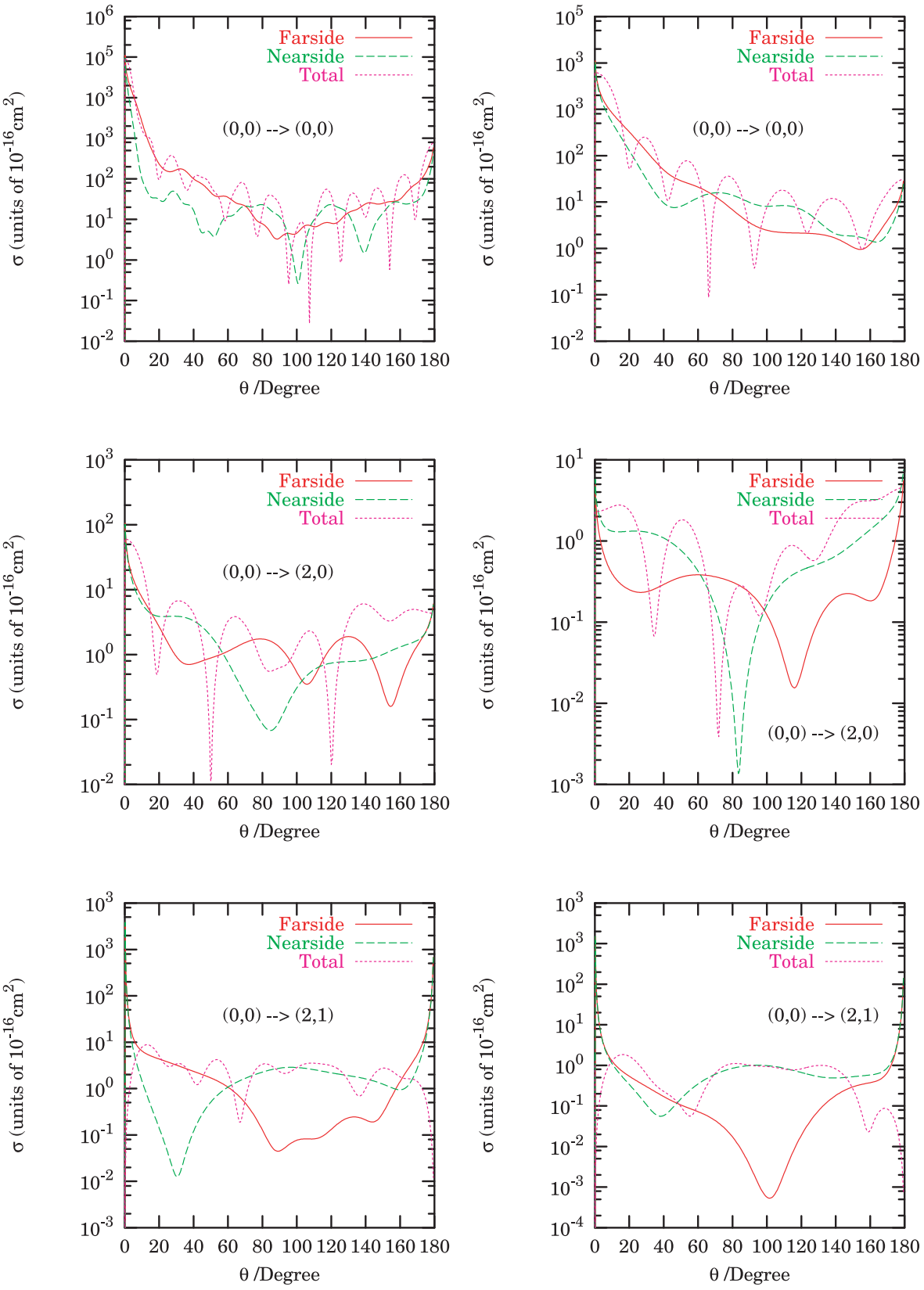

Fig. 7. (Color online) Differential cross-sections at $E = 20$ cm^{-1}, $\log(I(\theta))$ versus θ for the various transitions indicated in the figure in the He–N_2^+ and He–N_2 collisions. The collisions involving N_2^+ and N_2 are respectively on the left side and right side of the figure.

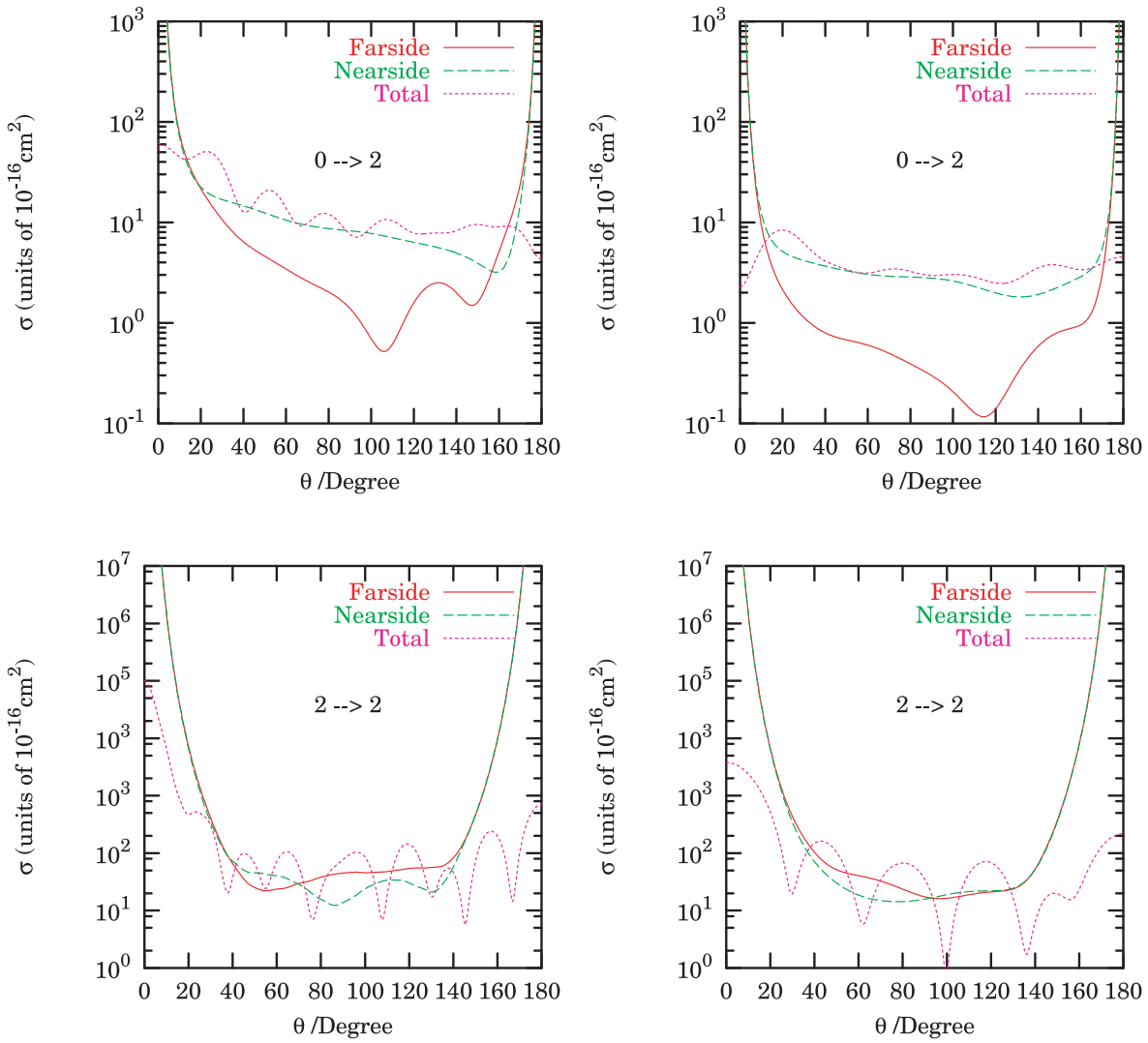

Fig. 8. (Color online) Degeneracy averaged differential cross-sections at 20 cm^{-1}, $\log(I(\theta))$ versus θ for the transitions indicated in the figure in the He–N_2^+ and He–N_2 collisions. The collisions involving N_2^+ and N_2 are respectively on the left side and right side of the figure.

The degeneracy averaged angular distributions reported in Figure 6 again are simpler. The angular interval where the two subamplitudes have comparable magnitudes extended considerably for He–N_2^+ whereas it is still limited for the He–N_2 collision and the resulting diffraction oscillations follow the same evolution.

4.3 E = 20 cm^{-1}

This energy was chosen because it is approximately the value of the well depth for He–N_2. We see in Figures 7 and 8 when comparing with the corresponding transitions at 100 cm^{-1} the same evolution described between 1000 cm^{-1} and 100 cm^{-1}. The angular domain where the collision is controlled by the farside component has extended again and the oscillations of the farside component have slow down and grown again in amplitude. The collision of both the neutral and the ionic species are now the result of the strong interaction of the two sub amplitudes. Inside a given transition the difference between the nearside and farside sub amplitudes increases when Δm is increased and as a result, the degeneracy averaged inelastic cross-sections are still controlled by the nearside component in a large angular interval for both the collisions involving the neutral and the ionic specie.

4.4 Resonance

If we examine equations (1), (4) and (5) we see that when the single partial wave associated with a resonance is large compared to the background contributions the two nearside farside subamplitudes result in two equal contributions to the cross-section since they are complex conjugates of each other. The nearside farside analysis then gives a new picture of the resonance. At the resonance energy, there is equilibrium between the nearside and the

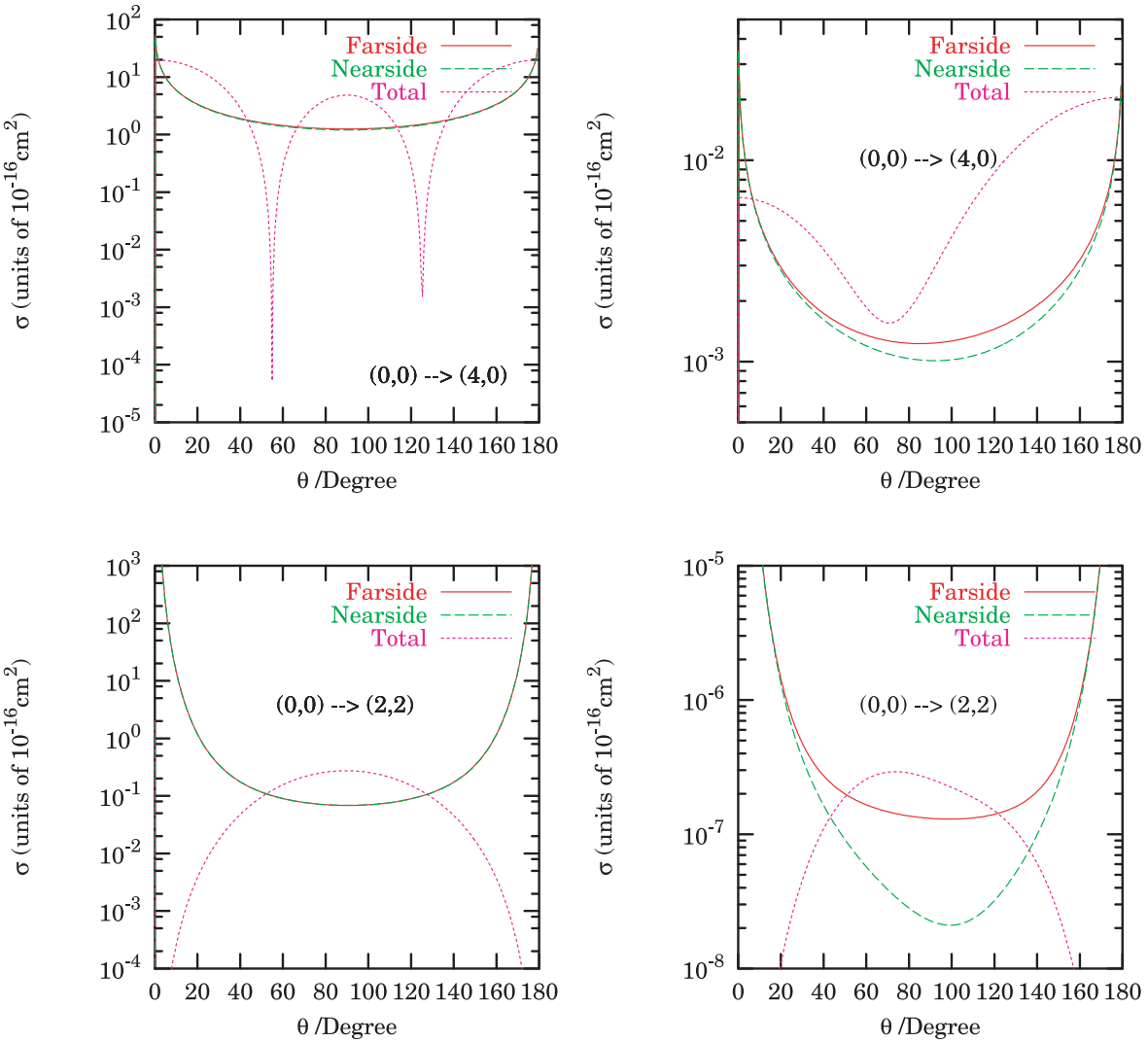

Fig. 9. (Color online) Differential cross-sections at 4.98×10^{-3} cm^{-1}, $\log(I(\theta))$ versus θ for the transitions indicated in the figure in the ^{3}He–N_2^+ and ^{4}He–N_2^+ collisions. The collisions involving ^{3}He and ^{4}He are respectively on the left side and right side of the figure.

farside subamplitudes (they are equal on the whole angular range). In other words, there is equilibrium between the repulsive and the attractive parts of the potential. This is indeed what can be seen in Figure 9 where we have drawn a very low energy $l = 2$ resonance for the ^{3}He–N_2^+ collision. We have chosen this example since at this collision energy the background scattering is negligible. This subtle equilibrium is easily broken and a change of mass from ^{3}He to ^{4}He is enough to remove the resonance for the ^{4}He–N_2^+ collision. The nearside farside analysis give a clear picture of the breaking of this equilibrium as can be seen on the same figure where the two collisions are compared at the same energy. (^{3}He–N_2^+ on the left side and ^{4}He–N_2^+ on the right side.) The two nearside and farside subamplitudes of the cross-sections are equal on the whole angular interval for the ^{3}He–N_2^+ collision while they differ strongly for the ^{4}He–N_2^+ collision.

5 Conclusion

The application of the nearside farside analysis to the comparison between the He–N_2^+ and He–N_2 inelastic collisions sheds a new light on the dynamics of these two collisions. Not only the usual tendencies predicted approximately by a semi classical approach are very simply obtained here exactly from a full quantum close coupling approach but more detailed information about the balance between the roles played by the repulsive and attractive parts of the intermolecular potential as a function of energy is also easily produced. At the highest energy (1000 cm^{-1}) the dynamics appears to be controlled essentially by the nearside component of the cross-section which is associated with the repulsive core of the potential, while the farside component of the cross-section associated with the attractive long range part and the well, is only at the origin of small additional oscillations in the general "rotational rainbow"

profile given by the nearside component associated with the repulsive heart. As a result the angular scattering is essentially the same for the two collisions since the repulsive part of the potentials are very similar. When the energy is decreased, the angular domain where the collision is controlled by the farside component is increased and the oscillations of the farside component slow down and grow in amplitude. The collision of both the neutral and the ionic species become the result of the strong interaction of the two sub amplitudes. In this regime the differences between the Van der Waals wells make the angular scattering differ for these two collisions. Inside a given transition the difference between the nearside and farside sub amplitudes increases when Δm is increased and as a result, the degeneracy averaged inelastic cross-sections are still controlled by the nearside component and inelastic scattering is then still controlled by the repulsive core in a large angular interval. At the resonance energy and for the partial wave associated with the resonance, there is an equilibrium between the nearside and the farside subamplitudes (they are equal on the whole angular range). The nearside farside analysis then gives a new picture of a resonance which is regarded as an equilibrium between the repulsive and the attractive parts of the potential.

We thank Pr Connor for encouraging us to get acquainted with the nearside farside method on the other side of the Channel.

References

1. P. McCabe, J.N.L. Connor, J. Chem. Phys. **104**, 2297 (1995)
2. F.L. Schöier, F.F.S. van der Tak, E.F. van Dishoeck, J.H. Black, A&A **432**, 369 (2005); M.L. Dubernet, Database: `http://www.obspm.fr/basecol`
3. J. Doyle, B. Friedrich, R.V. Krems, F. Masnou-Seeuws, Eur. Phys. J. D **31**, 149 (2004)
4. R.V. Krems, Int. Rev. Phys. Chem. **24**, 99 (2005)
5. P. McCabe, J.N.L. Connor, D. Sokolowski, J. Chem. Phys. **108**, 5695 (1998)
6. T.W.J. Whiteley, C. Noli, J.N.L. Connor, J. Phys. Chem. **105**, 2792 (2001)
7. P. McCabe, J.N.L. Connor, D. Sokolowski, J. Chem. Phys. **114**, 5194 (2000)
8. R.C. Fuller, Phys. Rev. C **12**, 1561 (1975)
9. P.J. Hatchell, Phys. Rev. C **40**, 27 (1989)
10. T. Stoecklin, A. Voronin, J.C. Rayez, Phys. Rev. A **66**, 42703 (2002)
11. T. Stoecklin, A. Voronin, Phys. Rev. A **72**, 042714 (2005)
12. M. Jacob, G. Wick, Ann. Phys. (N.Y.) **7**, 404 (1959)
13. D. Sokolowski, J.N.L. Connor, Chem. Phys. Lett. **305**, 238 (1999)
14. F.J. Aoiz, L. Banares, V.J. Herrero, B. Martinez-Haya, M. Menedez, P. Quintana, I. Tanarro, E. Verdasco, Chem. Phys. Lett. **367**, 500 (2003)
15. A.S. Dickinson, W.K. Liu, Mol. Phys. **93**, 789 (1998)
16. W.R. Rodwell, L.T. Sim Fai Lam, R.O. Walts, Mol. Phys. **44**, 225 (1981)
17. A.M. Sapse, J. Chem. Phys. **78**, 5733 (1983)
18. M. Raimondi, Mol. Phys. **53**, 161 (1984)
19. D.E. Woon, T.H. Dunning Jr, J. Chem. Phys. **98**, 1358 (1993)
20. T.S. Ho, H. Rabitz, J. Chem. Phys. **104**, 2584 (1996)
21. C. Reese, T. Stoecklin, A. Voronin, J.C. Rayez, A&A **430**, 1139 (2005)
22. T. Stoecklin, A. Voronin, J.C. Rayez, Phys. Rev. A **68**, 032716 (2003)
23. T. Stoecklin, A. Voronin, J.C. Rayez, Chem. Phys. **298**, 175 (2004)
24. R.W. Anderson, J. Chem. Phys. **77**, 4431 (1982); E.B. Stechel, R.B. Walker, J.C. Light, J. Chem. Phys. **69**, 3518 (1978)
25. J.M. Launay, J. Phys. B **10**, 3665 (1977)
26. T. Colbert, W.H. Miller, J. Chem. Phys. **96**, 1982 (1992)
27. F.A. Gianturco, A. Palma, J. Chem. Phys. **83**, 1049 (1985)
28. J.N.L. Connor, D. Farrely, D.C. Mackay, J. Chem. Phys. **74**, 3278 (1981); K.E. Thylwe, J.N.L. Connor, J. Chem. Phys. **91**, 1668 (1989)
29. R.B. Bernstein, J.T. Muckerman, Adv. Chem. Phys. **12**, 389 (1967)